Journal of Alloys and Compounds 961 (2023) 171045

Contents lists available at ScienceDirect

Journal of Alloys and Compounds

journal homepage: www.elsevier.com/locate/jalcom

# Co-precipitated vanadium oxide-doped carbon spheres and graphene oxide nanorods serve as antimicrobial and catalytic agents: In silico molecular docking study

Muhammad Ikram [a,*], Muhammad Shahid Ali [b], Ali Haider [c], Iram Shahzadi [d], Muhammad Mustajab [a], Anwar Ul-Hamid [e], Anum Shahzadi [f], Walid Nabgan [g,*], Mohammed M. Algaradah [h], Ahmed M. Fouda [i], Salamat Ali [j]

[a] Solar Cell Applications Research Lab, Department of Physics, Government College University Lahore, 54000, Pakistan
[b] Department of Physics, Riphah Institute of Computing and Applied Sciences (RICAS), Riphah International University, 14 Ali Road, Lahore, Pakistan
[c] Department of Clinical Sciences, Faculty of Veterinary and Animal Sciences, Muhammad Nawaz Shareef University of Agriculture, Multan 66000, Pakistan
[d] Punjab University College of Pharmacy, University of the Punjab, Lahore 54000, Pakistan
[e] Core Research Facilities, King Fahd University of Petroleum & Minerals, Dhahran 31261, Saudi Arabia
[f] Faculty of Pharmacy, The University of Lahore, Lahore 54000, Pakistan
[g] Departament d'Enginyeria Química, Universitat Rovira i Virgili, Av Països Catalans 26, 43007 Tarragona, Spain
[h] Chemistry Department, King Khalid Military Academy, Riyadh 11495, Saudi Arabia
[i] Chemistry Department, Faculty of Science, King Khalid University, Abha 61413, Saudi Arabia
[j] Department of Physics, The University of Lahore, Lahore 54000, Pakistan

ARTICLE INFO

*Article history:*
Received 5 April 2023
Received in revised form 15 June 2023
Accepted 17 June 2023
Available online 19 June 2023

*Keywords:*
Vanadium oxide
Antimicrobial activity
Rhodamine B degradation
Molecular docking analysis
Co-precipitation

ABSTRACT

Undoped $V_2O_5$ is characterized by a small surface area and rapid electron-hole recombination, thus rendering it ineffective as a catalytic and antimicrobial agent. In this study, co-precipitation was employed to synthesize vanadium oxide ($V_2O_5$) and carbon spheres (CS) followed by doping with specific concentrations (3 and 6 wt%) of graphene oxide (GO) to produce GO/CS-doped $V_2O_5$ nanorods (NRs). The enhancement in catalytic and antibacterial activity provided by GO/CS-doped $V_2O_5$ was utilized to treat wastewater more efficiently. XRD analysis validated the orthorhombic and tetragonal structure of the synthesized samples. The polycrystalline nature of $V_2O_5$ was shown by vibrant circular rings in selected area electron diffraction (SAED) micrographs. TEM analysis endorsed formation of NRs, whereas UV–vis, luminescence (PL) and fourier transform infrared spectroscopy (FTIR), probed the absorption and emission along with stretching and bending vibrations in V-O-V bond. The chemically synthesized NRs exhibited excellent catalytic activity (93.71%) against rhodamine B (RhB) dye in the vicinity of $NaBH_4$. In addition, NRs were used to evaluate *in-vitro* antimicrobial efficiency of 3.75 mmfor *Escherichia coli* (*E. coli*) using inhibition zone measurement. Docking investigations of GO/CS-$V_2O_5$ NRs for FabH and FabI of *E. coli* suggested suppression of above-mentioned enzymes as a possible mechanism. These findings demonstrate that (3 and 6 wt%) GO/CS-$V_2O_5$ possessed ample potency for industrial dye degradation and antimicrobial activity.


## 1. Introduction

The extensive use of heavy metals and toxic dyes has led to an increase in water contamination on a large scale, which can be considered a by-product of ongoing rapid industrialization. The water pollution poses a significant risk to the natural ecosystem [1]. Toxic metallic particles (Cu, Cr, Ag, and Hg) are byproducts of ever-expanding chemicals, leather, paper, textile, and printing industries, which have polluted both human and aquatic biodiversity. The abundant use of many different textile manufacturing methods result in the production of a variety of dyes [2]. Organic dyes are resistant to chemical and biological breakdown by virtue of their sturdy and intricate chemical frameworks. Organic rhodamine B dye of xanthene class has widespread applications in textile, printing, food, and pharmaceutical industries [3]. Synthetic dyes and pollutants seriously threaten the health of both humans and animals [4]. The dyes can be degraded by a variety of processes, including electrochemical activity [5], catalytic activity,

* Corresponding authors.
*E-mail addresses:* dr.muhammadikram@gcu.edu.pk (M. Ikram), walid.nabgan@urv.cat (W. Nabgan).

https://doi.org/10.1016/j.jallcom.2023.171045

photocatalytic activity (PCA)) [6], etc. Catalytic activity of nanorod-based semiconductor materials has sparked the curiosity of researchers owing to their low toxicity, eco-friendly nature, chemical durability, and cost-effectiveness [7]. A reducing agent and a nanocatalyst break down rhodamine B (RhB) as well as other synthetic dyes [8]. Moreover, disorders such as Mastitis may be driven by an assortment of bacteria, viruses, and fungi. Mastitis has a substantial economic burden on the dairy industry. Clinical anomalies in mammary gland tissues and chemical, microbiological, and physical variations in the milk are all associated with this disorder [9].

Transition metal oxide nanoparticles such as CuO, $Fe_2O_3$, ZnO, $MnO_2$, and $V_2O_5$ have been widely employed for water purification [10–13] since these materials have a large surface area, excellent chemical stability, and high recyclability without secondary pollutant production [14]. Applications for dye degradation have employed $V_2O_5$ nanoparticles due to their non-toxicity, small band gap (2.4–2.8 eV), and enhanced electro-chemical integrity [14]. However, $V_2O_5$ has significant limitations as a photocatalyst in aqueous electrolytes due to photo and electrochemical corrosion [15]. The electrochemical corrosion properties may be improved in a number of ways; by mixing with conductive matrix or semiconductor materials to increase its surface activity [16]. Photo-induced electron-hole pairs may be better separated and photo corrosion can be reduced by forming a heterostructure while interfacing a semiconductor to another material with a similar band potential [17].

Carbon spheres have also received much interest in catalysis field considering their high specific area, low density, as well as improved CA [18]. Carbon spheres are known to stabilize metal oxide compounds for efficient dye degradation due to their quick and efficient reduction ability [19,20]. Graphene, a bi-dimensional (2D) substance comprised of layers of carbon atoms stacked into a honeycomb network, piqued the curiosity of scientists through its excellent charge carrier mobility, abundant defect sites, vast surface area and superior electrical and optical conductivities have gained very remarkable attention in the treatment of wastewater containing heavy metal ions and dyes [21,22]. Graphene oxide (GO) is useful in energy conversion, storage, and catalytic activities owing to its high hydrophilicity, reaction activity [23,24], and availability of functional groups on surfaces, including epoxy groups, carboxyl groups, hydroxyl groups, and carbonyl groups [25]. $V_2O_5$ material is a diverse catalyst of brookite $TiO_2$ and orthorhombic $V_2O_5$ phases formed by mechanical alloying and demonstrating ~76% RhB degradation. $TiO_2$–$V_2O_5$ nanocomposite showed dye degradation efficacy of ~89% with $H_2O_2$[26]. However, in the current work, doping-dependent $V_2O_5$ NRs were examined for their ability to degrade the pollutant RhB without light using $NaBH_4$.

This study aims to synthesize (3 and 6 wt%) GO/CS-$V_2O_5$ NRs using an environmentally acceptable co-precipitation approach for degradation of organic dyes and to evaluate its bactericidal capability. The antibacterial effectiveness of NRs was also evaluated in comparison to ciprofloxacin using E. coli. Various characterization approaches were employed for a comprehensive study of synthesized NRs.

## 2. Experimental section

### 2.1. Materials

Ammonium metavanadate ($NH_4VO_3$), nitric acid ($HNO_3$), hydrogen peroxide ($H_2O_2$), polyvinylpyrrolidone (PVP), glucose, and graphite were acquired from Sigma Aldrich, and all the reagents used in this process were of analytical grade, so there was no need for further purification.

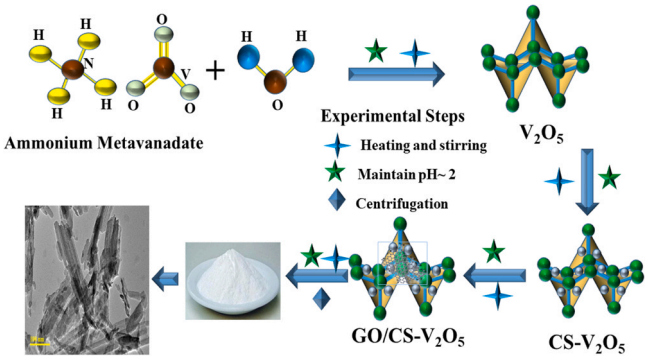


**Fig. 1.** Schematic illustration of synthesized pristine and GO/CS-$V_2O_5$.

### 2.2. Synthesis of carbon spheres/graphene oxide doped vanadium oxide

The co-precipitation technique to fabricate carbon spheres and graphene oxide-doped vanadium oxide is represented in Fig. 1. Initially, 0.5 M of ammonium metavanadate was heated and stirred constantly for 30 min. Nitric acid was injected in proper concentration to maintain pH~2 resulting in precipitate formation. For the transparent solution, a fixed amount (0.350 g) of PVP was incorporated, and the solution was vigorously mixed and heated for nearly 2 h around 90 ºC. The obtained precipitates were centrifuged at 7000 rpm to eliminate impurities by rinsing with deionized water (DI water). The washed sediments were heated at 150ºC to obtain the fine powders. The above-mentioned method was adopted to synthesize graphene oxide (3 and 6 wt.%) doped $V_2O_5$ with predetermined concentration of carbon spheres.

### 2.3. Catalytic activity (CA)

The catalytic activities for pure and GO/CS-doped $V_2O_5$ NRs were used to evaluate the degradation efficacy of RhB dye. In order to spectrophotometrically analyze the degradation of dye in 200–800 nm region, new solutions of RhB and sodium borohydride ($NaBH_4$) were created. 3 mLRhB (oxidizing agent) solution was incorporated with 400 µL $NaBH_4$ (reducing agent) solution and 400 µL pristine and GO/CS-doped $V_2O_5$ NRs. UV-Vis spectrophotometer was employed to measure absorption variation spectra at periodic intervals. The % degradation was measured by degradation (%) = $(C_o-C_t)/C_o \times 100$, where $C_o$ represents initial dye concentration and $C_t$ is the dye concentration at a specific time after addition of materials.

### 2.4. Isolation and identification of MDR E. coli

#### 2.4.1. Isolation of E. coli

The unpasteurized milk samples were collected from the lactating dairy cows sold at various marketplaces, such as veterinary hospitals and dairy farms in Punjab, Pakistan. For immediate milking, clean glass containers were used. A lab collected the raw milk sample at 4 ºC directly after it was collected from the marketplace. MacConkey agar was employed and incubated at 37 ºC for 48 h in petri dishes to count the coliforms in fresh milk.

#### 2.4.2. Identification and characterization of E. coli

Gram colonial morphology, several biochemical assays, and a relation to Bergey's Manual of Determinative Bacteriology were utilized to determine the initial diagnosis of *E. coli* [27].

*2.4.2.1. Antibiotic susceptibility*. Mueller Hinton agar (MHA) was examined for antibiotic susceptibility of bacteria using the disc diffusion method [28]. Antibiotic resistance of gram-ve (*E. coli)*

bacteria was evaluated towards the following antibiotics (classes); Azithromycin (Azm) 15 µg (Macrolides), Ciprofloxacin (Cip) 5 µg (Quinolones), Gentamicin (Gm) 10 µg (Aminoglycosides), Ceftriaxone (Cro) 30 µg (Cephalosporins), Amoxycillin (A) 30 µg (Penicillin), Imipenem (Imi) 10 µg (Carbapenem) and Tetracycline (Te) 30 µg (Tetracyclines)[29]. *E. coli* cultures were grown, and a turbidity level of 0.5 MacFarland standard was obtained. It was then disseminated throughout MHA (Oxoid Ltd, Basingstoke, UK), and antibiotic discs were placed extensively over the inoculation plate's surface. It was applied to prevent inhibition zones from being disturbed. The results were analyzed after 48 h of culture at 37 °C [30]. MDR microorganisms have been identified against antibiotic resistance to at least three antibiotics [31].

*2.4.2.2. Antimicrobial activity*. The antibacterial potential of pristine $V_2O_5$ and (3 and 6 wt%) GO/CS-$V_2O_5$ were evaluated to calculate inhibition areas for MDR *E. coli*viaagar diffusion assay. MDR *E. coli* has been inoculated onto agar plates at a concentration of $1.5 \times 10^8$ CFU/mL (0.5 McFarland standards) on MacConkey agar. *E. coli* was routinely isolated from animal mastitis fluid for bacterial effectiveness of pure and doped materials. After disinfecting agar plates, 6 mm diameter pores were drilled via borer to test the pathogenic microorganisms. Ciprofloxacin 5 µg/50 µL and DI water 50 µL were used as positive and negative controls, separately. The boreholes were filled with host and varied concentration levels of the doped NRs at both concentrations of 0.5 mg/50 µL and 1.0 mg/50 µL, respectively. Plates were kept at room temperature overnight and inhibited zones were measured by Vernier caliper. Diameters (mm) of inhibitory zones of synthesized NRs were measured for antimicrobial activity [32].

*2.4.2.3. Statistical analysis*. The antibacterial efficacy was determined by measuring inhibitory zones diameters using one-way analysis of variance (ANOVA) in SPSS 20 [33].

### *2.5. Molecular docking analysis*

The putative mechanism of CS-$V_2O_5$ and GO/CS-$V_2O_5$ was estimated by in *silico* docking, an effective technique to assess microbicidal activity. Antibiotics that target the fatty acid biosynthesis enzyme, β-ketoacyl acyl carrier protein synthase III (FabH) and Enoyl-[acyl-carrier-protein] reductase (FabI), have been predicted as viable alternatives. We exploited 3D structural attributes from Protein Data Bank and designed via protein synthesis software to successfully bind GO/CS-$V_2O_5$ NRs into the active site. The target access numbers were 4D46 (Resolution: 2.0) (FabI) [34] and 5BNR (Resolution: 1.7) for FabH[35], respectively. Similar to our previous investigations, SYBYL-X 2.0 was used for 3D structures to analyze binding affinities with active residues of specific proteins [36,37].

## 3. Results and discussion

$V_2O_5$ and GO/CS-doped $V_2O_5$ NRs were synthesized via co-precipitation using ammonium metavanadate. Various concentrations of GO and fixed concentrations of CS were put into the solution containing $NH_4VO_3$ to synthesize GO/CS-doped $V_2O_5$ NRs(Fig. 1**).**

X-ray diffraction (XRD) analysis was used to assess crystal structure, phase composition, crystal size, crystallinity, and interplanar characteristics for undoped $V_2O_5$ and (3 and 6 wt%) GO/CS-$V_2O_5$ in the range of 20°-60°(Fig. 2a). The XRD spectra reveal seven major diffraction peaks at angle 2θ values 21.7°, 26.2°, 28.37°, 34.4°, 41.3°, 51.3° and 58.7° with the corresponding (110), (101), (033), (301), (020), (002), and (611) crystalline planes, respectively. Pristine and GO/CS-doped $V_2O_5$ exhibit the orthorhombic and tetragonal crystal structure, with the phase composition of vanadium oxide having space group Pmn21 and P E that is well matched with the standard JCPDS card # (01–076–1803, 00–045–1074). CS-doped $V_2O_5$ showed prominent peaks at diffraction angle 2θ values 31.1° and 44.7° with corresponding crystal (400) and (510) planes synchronized with the JCPDS card No. 01–076–1803. The shift of peaks towards higher angle and the appearance of a few new peaks indicate an improvement in crystallinity. Upon higher GO concentrations, the intensity of a diffraction peak increased, suggesting the crystalline nature of the materials. The high crystalline nature can be confirmed with intense and high diffraction peaks. The poor crystalline structure of carbon accounts for wide, low-intensity peaks was seen in diffraction patterns of CS and GO. However, the higher-order crystalline character of the orthorhombic structure was verified by the diffraction pattern of $V_2O_5$ rods [38]. The average crystallite sizes of pure and (3 and 6 wt%) GO/CS-$V_2O_5$ NRs were determined using Scherrer's formula and calculated as 55, 65, 78, and 83 nm, respectively. Hence, the average crystallite size also increases gradually with an increasing concentration of dopants. The tiny crystallite size and poor crystallization of the vanadium pentoxide are reflected in peaks' high sharpness and broadness. After doping, the peak intensity of undoped sample increased, indicating high crystallinity and increased crystallite size. In the case of CS and GO, the XRD pattern differs from the bare $V_2O_5$ NRs observed in the previous study [39]. When the concentration of dopants was raised, the atoms rearranged themselves in a way that changed location of $2\theta$ to the left and boosted its intensity. Furthermore, full width at half maxima (FWHM) became smaller and the crystal size increased upon increase in doping concentration. For high doping concentrations, the pressures imposed on via dissimilar particle sizes of vanadium and dopant, as well as the segregation of dopants in grain boundaries, may contribute to an increase in the crystallinity of NRs[40].

FTIR analysis performed to identify the functional groups in pristine and GO/CS- $V_2O_5$ NRs in the 400–4000 $cm^{-1}$, is indicated in Fig. 2(b). The strong as well as weak bands observed around 3349 and 1655 $cm^{-1}$ are associated with O-H stretching vibrations and symmetric bending vibrations of water molecules, separately, that adsorbed from the atmosphere during sample preparation [41]. The band appearing nearby 996 $cm^{-1}$, was assigned to C-O stretching vibration from surroundings during sample preparation and also attributed to stretching vibrations of the termination V═O groups. The absorption bands at 570 [38] and 691 $cm^{-1}$ were assigned to asymmetric V-O-V vibrations that confirm the formation of $V_2O_5$ NRs [42,43]. Following the shift to lower wavenumber, bands detected for GO/CS-$V_2O_5$ NRs provide strong evidence that their structure is fundamentally different from $V_2O_5$. The significant interaction between doped and $V_2O_5$ nanorods is shown by the band shift towards lower energy region [38]. Crystallinity was determined for both pure and GO/CS-doped $V_2O_5$ NRs (Fig. 2c, d) using selected area electron diffraction (SAED) analysis. The bright spots combine to generate bright rings (concentric rings) that are polycrystalline. The indices of rings match perfectly with XRD data, providing compelling evidence that resulting products were extremely crystalline.

UV–vis spectra were recorded for optical absorption of pristine and GO/CS-doped $V_2O_5$ in 350–600 nm range (Fig. 3a). $V_2O_5$ exhibits an absorption peak at 400 nm. Absorption spectra show a redshift with the incorporation of CS/GO [44,45]. As the doping concentration increased, the redshift in the absorption edges was observed, revealing that $V_2O_5$ had higher optical activity in the visible region [46]. Absorption of GO/CS-doped $V_2O_5$ is accompanied by a redshift, implying morphological effects with many active sites or a quantum confinement effect. Absorption in higher wavelengths was detected after doping with CS/GO and attributed to decreased band gap energy (Eg). The Eg was calculated using the Tauc relation $(\alpha h\nu)^2$, and the extrapolated value of the line for pristine specimen was 3.1 eV. The higher concentration of CS/GO, Eg has been reduced from 3.1 to 2.87 eV(Fig. 3b). This decrease in bandgap energy upon doping can

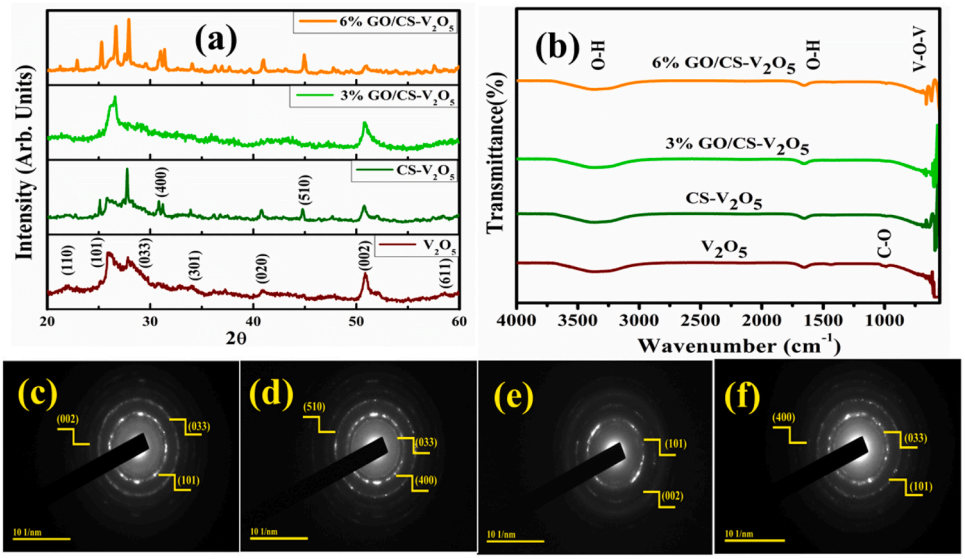


**Fig. 2.** (a) X-ray diffraction pattern of GO/CS-$V_2O_5$ NRs, (b) FTIR spectra of doped $V_2O_5$, and SAED images of $V_2O_5$ (c), CS-$V_2O_5$ (d) 3 wt% GO doped CS-$V_2O_5$ NRs (e) 6 wt% GO doped CS-$V_2O_5$ NRs (f).

be attributed to the shift of the absorption edge to higher wavelengths (redshift).

PL emission spectra of synthesized specimen were examined to regulate the variations in charge-transfer efficiency and recombination rate. Once electrons inside VB are accelerated to a CB during an emission peak but revert to the VB, a photoluminescence spectrum is generated [47]. The control sample exhibits a single brilliant green emission band at 548 nm [48,49] that can be represented in Fig. 3 (c). A pristine sample demonstrates the highest intensity, high recombination, and lowest electron transfer efficiency rate. Peak intensity reduced after doping, indicating a lower charge carrier recombination, but increased as GO content increased, indicating a strong preference for a photo-generated charge carrier [50]. PL intensity decreased, suggesting a slower $e^-$– $h^+$ recombination rate, increasing the excited charge carriers' duration. The highest intensity can be observed in undoped nanostructures with a high $e^-$– h+ pair recombination rate. With the addition of CS/GO, the peak intensity decreased, which caused a decrease in electron-hole recombination and increased the electron-hole transfer rate, which enhanced the degradation efficiency of dye.

SEM analysis for the surface morphology of doped $V_2O_5$ is represented in Fig. 4(a-d). The pure sample indicates the formation of clusters with aggregation and agglomeration of $V_2O_5$ constituents. The incorporation of CS and GO increased agglomeration, indicating the formation of chunk-like morphology and nanorods. As the

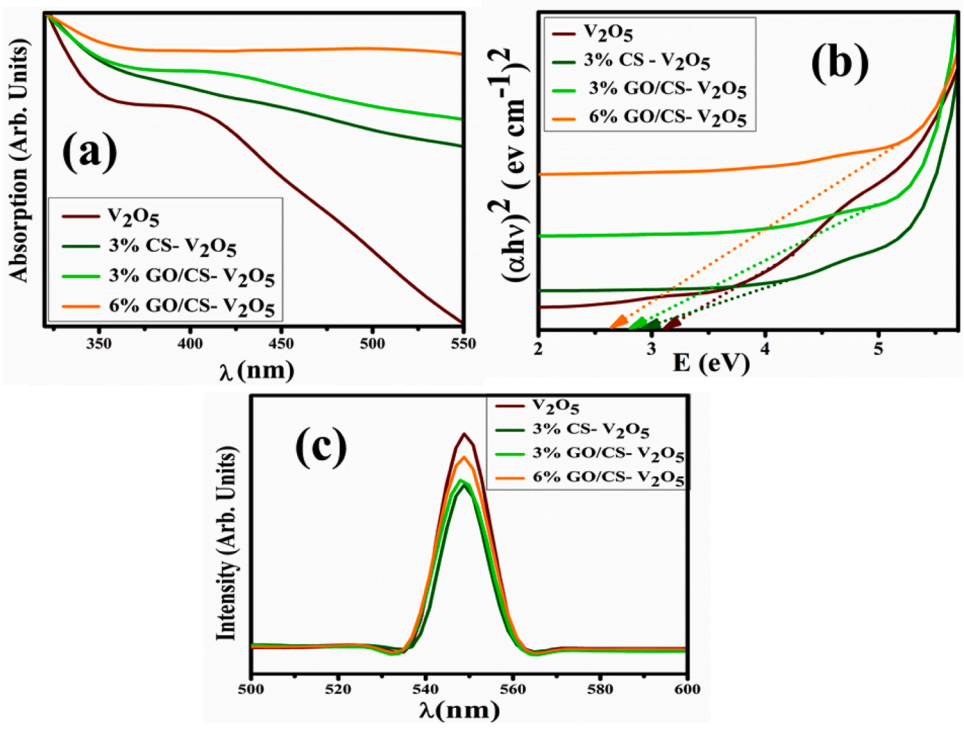


**Fig. 3.** (a) Absorption spectra, (b) band gap energy and (c) PL emissionspectra ofdoped $V_2O_5$.

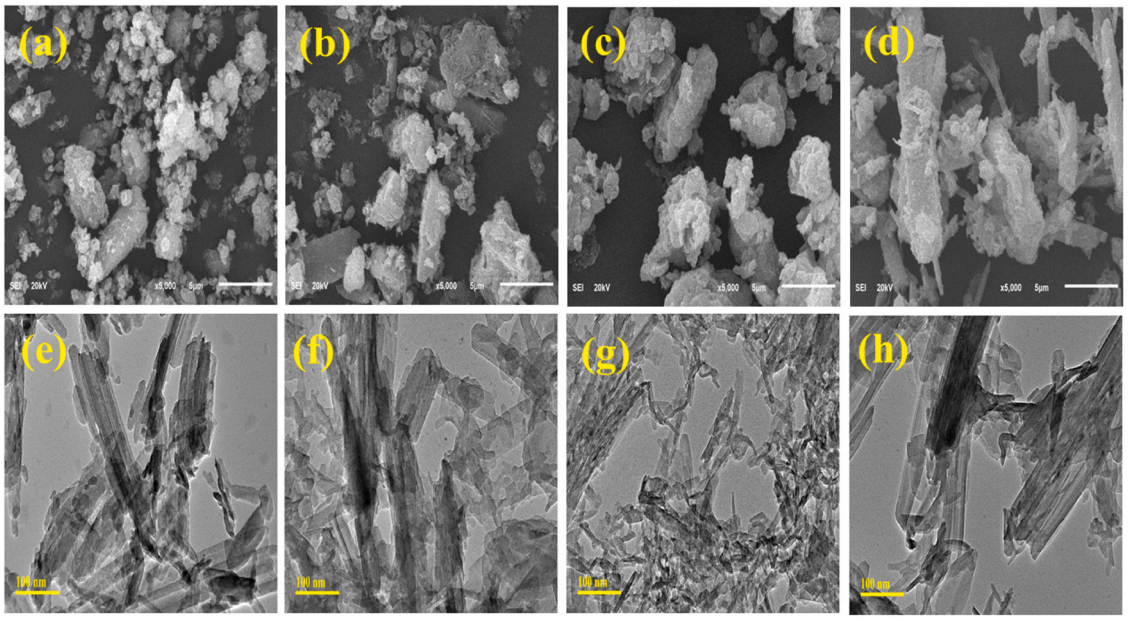


**Fig. 4.** (a-d) SEM micrograph of synthesized NRs (e-h) TEM micrograph of synthesized NRs.

doping concentration of GO/CS increased, the morphology of the nanorods and layers of sheet-like morphology were observed.

The topography, surface structure, and appearance of specimen were investigated using TEM Fig. 4(e-h). The $V_2O_5$ sample indicates the formation of nanorods with accumulation and aggregation of V and O at the atomic scale. The addition of CS in the control sample showed that agglomeration decreases and exhibits small nanorods proclaimed in CS-$V_2O_5$. With GO, the TEM images exhibited a smoother and more sheet-like morphology of nanorods. The agglomeration rises as the doping concentration of GO increases, indicating the sheet-like morphology of synthesized materials; additionally, nanorods emerge in the sheets.

HR-TEM morphology indicate interlayer D-spacing of synthesized NRs in Fig. 5(a-d). The interlayer D-spacing value was calculated via Gatan digital micrograph software onto HR-TEM micrographs. The D-spacing values of $V_2O_5$ and GO/CS-$V_2O_5$ were calculated as 0.15, 0.32, 0.31, and 0.31 nm for diffraction in the (002), (033), (240) and (240) planes that are synchronized with XRD measurements and JCPDS card numbers 01–076–1803, 00–045–1074.

EDS analysis validated the vanadium and oxygen existence in $V_2O_5$ nanopowders by analyzing their chemical composition (Fig. 6(a-d)). The appearance of vanadium and oxygen in all the prepared samples indicates the synthesized product's purity. The mapping analysis confirmed the presence of vanadium and oxygen elements with various color combinations for GO/CS-$V_2O_5$. The existence of molybdenum was revealed due to instrumental error indicated in Fig. 6(e-h).

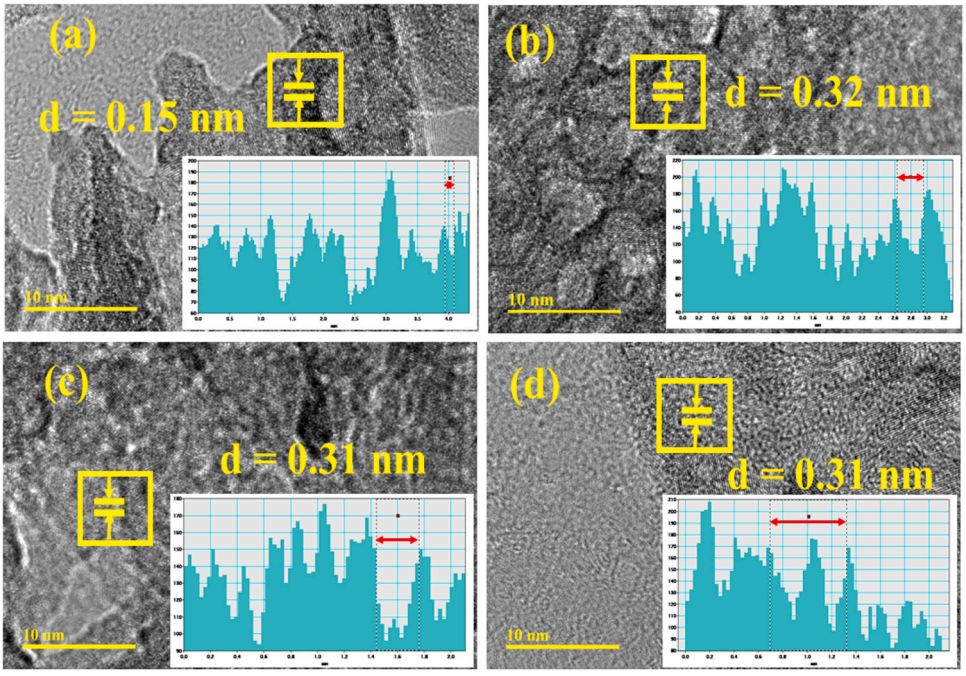


**Fig. 5.** The calculated interlayer D-spacing (a) $V_2O_5$ (b) CS-$V_2O_5$ (c) 3 wt% GO/CS-$V_2O_5$(d) 6 wt% GO/CS-$V_2O_5$.

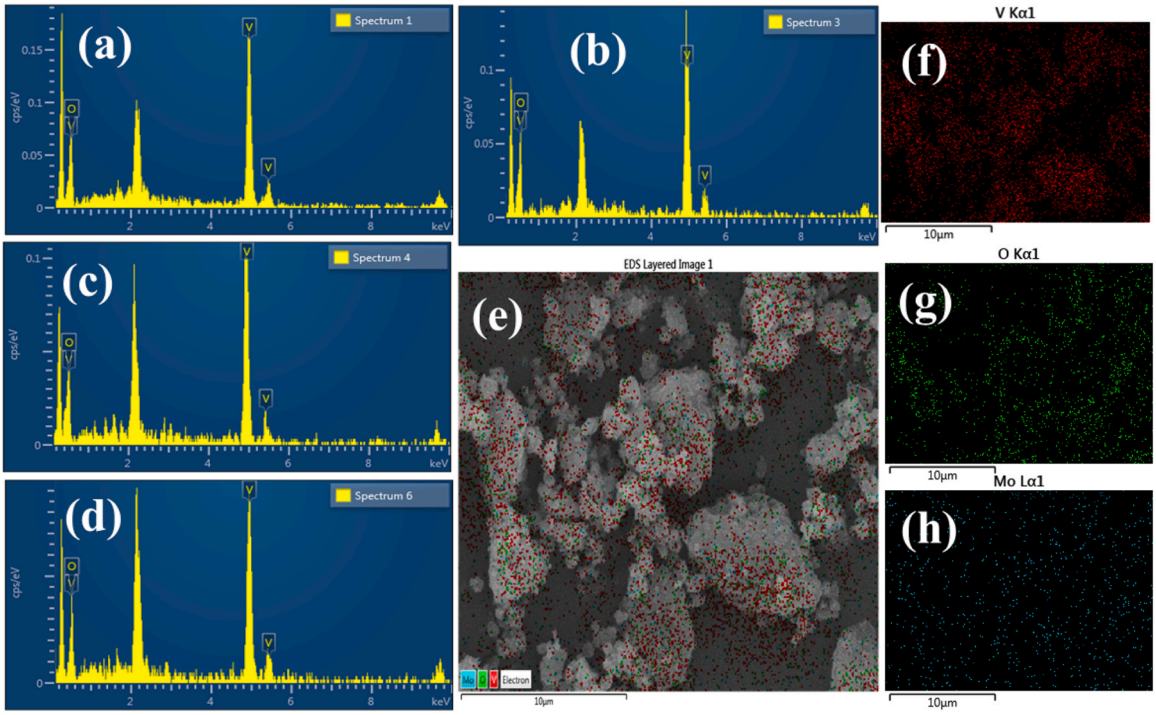


**Fig. 6.** (a-d) EDS Analysis of synthesized NRs and (e) Mapping analysis of prepared NRs (f) Vanadium (g) Oxygen (h) Molybdenum.

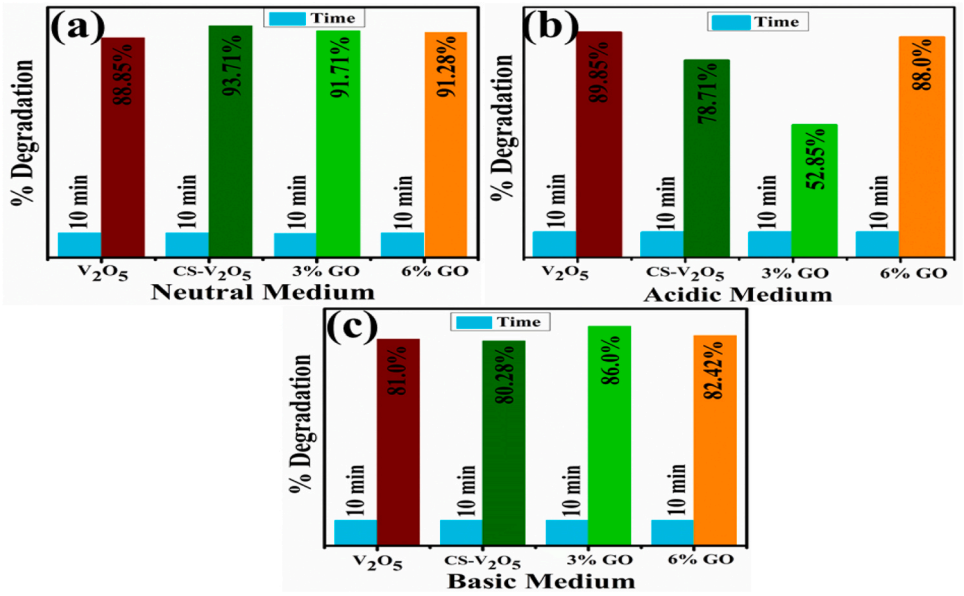


**Fig. 7.** Catalytic activity of pristine and (3 and 6 wt%) GO/CS-$V_2O_5$ in (a) Acidic, (b) Basic and (c) Neutral media.

**Table:1**
Literature comparison of degradation with current study.

| No. | Prepared sample | Synthesis method | Target dye | Degradation Performance | Refs. |
|---|---|---|---|---|---|
| 1 | $V_2O_5$ | Soft chemical method | Methylene blue (MB) | 92%. | [51] |
| 2 | $V_2O_5$ | hydrothermal | Methylene Orange | 82%, | [52] |
| 3 | $V_2O_5$-rGO | oxidation process | Rhodamine B (RhB) | 84% | [53] |
| 4 | g-$C_3N_4$/PAA-$V_2O_5$ | co-precipitation | RhB | 93.3 | [54] |
| 5 | GO/CS-$V_2O_5$ | co-precipitation | RhB | 93.7% | Present work |

The CA test was performed to degrade the RhB dye with $NaBH_4$, while synthesized NRs acted as electron shuttles between oxidizing and reducing agents for degradation. The degradation of RhB dye was investigated using synthesized catalyst $V_2O_5$ and GO/CS-doped $V_2O_5$with the help of UV–vis spectroscopy in 200–800 nm range. $V_2O_5$ and GO/CS doped $V_2O_5$ NRs exhibited maximum degradation against RhB dye at 88.85, 93.71, 91.71%, and 91.28% in neutral medium (pH = 7), 89.85%, 78.71%, 52.85% and 88% in acidic

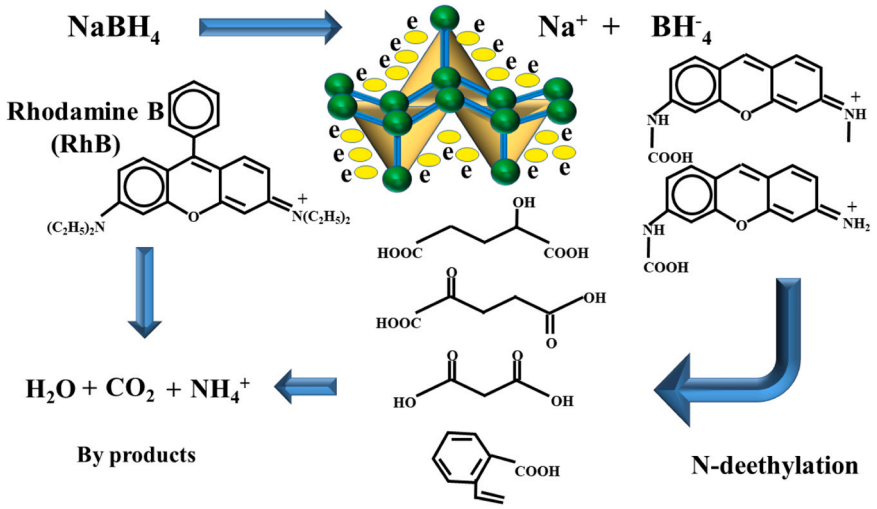


**Fig. 8.** Catalysis mechanism of the prepared NRs.

conditions (pH = 4) and 81.0%, 80.28%, 86.0% and 82.42% in basic medium (pH = 12), respectively(Fig. 7**a-c).** The comparison of present study with the literature of GO/CS-doped $V_2O_5$ NRs proved it to be a superior catalyst (Table 1). The highest catalytic efficiency was recorded in all three media. Due to its numerous roles, it is difficult to evaluate the pH effect on the effectiveness of the catalytic degradation of organic compounds. The first connection pertains to the surface acid-base properties of the metal oxides. The OH-charge group in water molecules breaks down when it comes into contact with chemically similar metal hydroxyl (M-OH) groups. The catalyst surface acquires a negative electrical charge as the pH of the solution rise because of the adsorption of OH ions. The production of OH free radicals, which are generally considered as the principal oxidizing species capable of degrading organic pollutants at neutral or high pH levels, is stimulated by the presence of large numbers of OH ions on the surface of the particles and in the reaction system. The study revealed that the basic and neutral zones eroded more quickly than the acidic medium [55].

The catalytic degradation of dye was observed by a redox reaction in which pure and GO/CS-doped $V_2O_5$ NRs act as a catalyst. The catalytic mechanism for the reduction of RhB can be proclaimed in Fig. 8. The redox reaction occurs between chemical substances RhB and $NaBH_4$ where an electron is transferred from donor to acceptor atoms. The nucleophilic $NaBH_4$ donates electrons to the NRs, whereas the electrophilic RhB may take electrons from the NRs to produce their equivalent reduction. The higher surface area of NRs necessitates a lower $NaBH_4$ loading. Upon higher concentrations of dopants in $V_2O_5$ NRs, the RhB degradation reaction rate increases exponentially in a neutral medium.

RhB degradation typically included N-deethylation and conjugated structure disintegration [56,57]. The % degradation of RhB rapidly accelerated, accompanied by a color change from pink to nearly colorless, demonstrating the loss of conjugated xanthene ring in the structure of RhBdye[58,59]. Benzenoid removal intermediates with mass divided by charge (*m/z*) values of 222, 157, 148, and 147 were also found, confirming fragmentation of RhB's conjugated xanthene structure [60,61]. The *m/z* values 268 and 254 corresponded to N-deethylated intermediates [62,63]. The intermediates mentioned above might be further reduced into different products with *m/z* values of 148, 118, and 104, respectively [61,64,65]. Low molecular weight compounds could ultimately be degraded and mineralized to produce $CO_2$, $H_2O$, and other inorganic substances. A plausible mechanism for the degradation of RhB by GO/CS-doped $V_2O_5$ beads with $NaBH_4$ is illustrated in Fig. 8**.** As a consequence, the production of $^{\bullet}OH$ radical will be quenched which causes an increase in dye degradation efficiency. Furthermore, achieving a few more accessible sites to adsorb on the surface of nanocatalyst with the addition of GO somewhat improves the degrading efficiency [66,67].

The antibacterial efficiency of the hosts and (3 and 6 wt%) GO/CS-$V_2O_5$ NRs for *E. coli* was assessed using diffusion method. For *E. coli*, substantial inhibition regions determined at low and high concentrations; (2.05–2.85 mm) and (2.95–3.75 mm), respectively (Table 3) were compared to ciprofloxacin having inhibition zone of 8.45 mm, and DIW (0 mm). If $V_2O_5$ were in low concentrations, measurements show minimum inhibition zones, but maximum inhibition zones would be observed with high concentrations. According to these observations, 6% GO/CS-$V_2O_5$ NRs show improved bactericidal performance against *E. coli*[71]. The comparison of literature review and present work for antimicrobial activity of prepared GO/CS-doped $V_2O_5$ NRs catalyst can be seen in Table 2.

Reactive oxygen species (ROSs), which usually produce oxidative stress, may represent the main mechanism in the following reaction.

$$GO/CS\text{-}V_2O_5 + h\nu\ (photon) \rightarrow h^+\ (hole) + e^-\ (excited\ electron)$$

$$e^- + O_2 \rightarrow *O_2^-$$

$$h^+ + H_2O \rightarrow OH^- + H^+$$

$$\bullet O_2^- + H^+ \rightarrow \bullet HO_2$$

**Table 2**
Literature comparison with the current study for antimicrobial activity.

| No. | Prepared sample | Synthesis method | Target bacteria | Inhibition zone (mm) | Refs. |
|---|---|---|---|---|---|
| 1 | $V_2O_5$ | hydrothermal | *E. coli* | 19 | [68] |
| 2 | HAP/$V_2O_5$/GO | co-precipitation | *E. coli* | 17.1 | [69] |
| 3 | Gd–$V_2O_5$/RGO | wet chemical | *S. aureus* | 14 | [70] |
| 4 | g-$C_3N_4$/PAA-$V_2O_5$ | co-precipitation | *E. coli* | 6.65 | [54] |
| 5 | GO/CS-$V_2O_5$ | co-precipitation | *E. coli* | 3.75 | Present work |

**Table 3**
Antibacterial potential of $V_2O_5$ and (3 and 6 wt%) GO/CS-$V_2O_5$ NRs.

| Samples | *E. coli* | |
|---|---|---|
| | Inhibition zone (mm) | |
| | 0.5 mg/50 $\mu$L | 1.0 mg/50 $\mu$L |
| $V_2O_5$ | 2.05 | 2.95 |
| CS -$V_2O_5$ | 2.30 | 3.15 |
| 3% GO/CS-$V_2O_5$ | 2.55 | 3.45 |
| 6% GO/CS-$V_2O_5$ | 2.85 | 3.75 |
| Ciprofloxacin | 8.45 | 8.45 |
| DI water | 0 | 0 |

$$\bullet HO_2 + e^- + H^+ \rightarrow \cdot H_2O_2$$

$$\cdot H_2O_2 + \bullet O_2^- \rightarrow \bullet OH + O_2 + OH^-$$

Radicals that can affect cell DNA and proteins include hydroxyl (•OH), superoxide ($O_2$•), and hydrogen peroxide ($H_2O_2$). Here, GO/CS-$V_2O_5$ NRs served as the generator of the ROSs released that increases the zone of inhibition[72].

The reaction [73] represents the mechanistic response of antimicrobial activity, where ROS plays an essential part in the killing of pathogenic bacteria (Fig. 9**).** Direct exposure with produced substance damages the cell wall and membrane of bacteria, leading to their mortality. When NRs generate intracellular ROS and interact with an organism's nucleic acid, they disclose their antimicrobial action by causing single and double-strand ruptures in nucleic acid's nitrogenous base and sugar-phosphate bond [74]. This is performed by boosting the oxidation of remaining amino acids and disconnecting critical proteins, interrupting a wide range of metabolic activities[75]. This suggests that reactive oxygen species (ROS) may be harmful to nucleic acid, and DNA damage in bacterial cells [76]. The interaction of electrostatic charge and bacterial membrane causes lysis and cell collapse. This contact eventually results in the death of the microorganisms involved. NRs destroy bacteria better at higher concentrations[77].

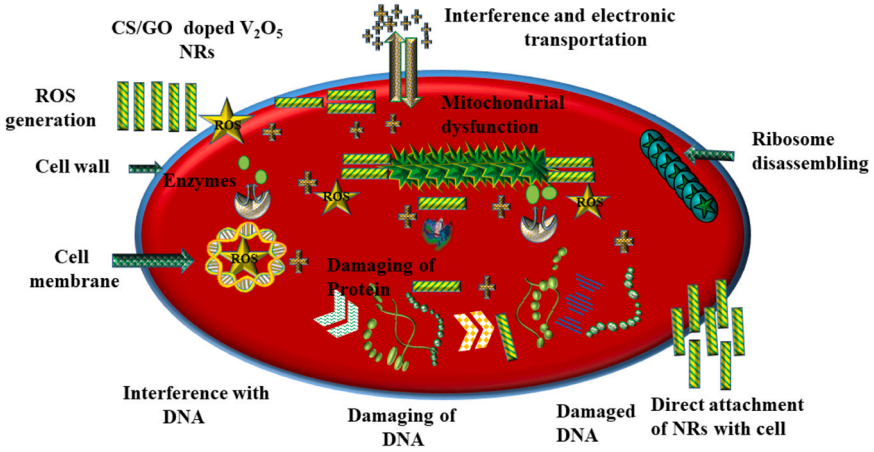


**Fig. 9.** Schematic mechanism of antimicrobial activity of the prepared NRs.

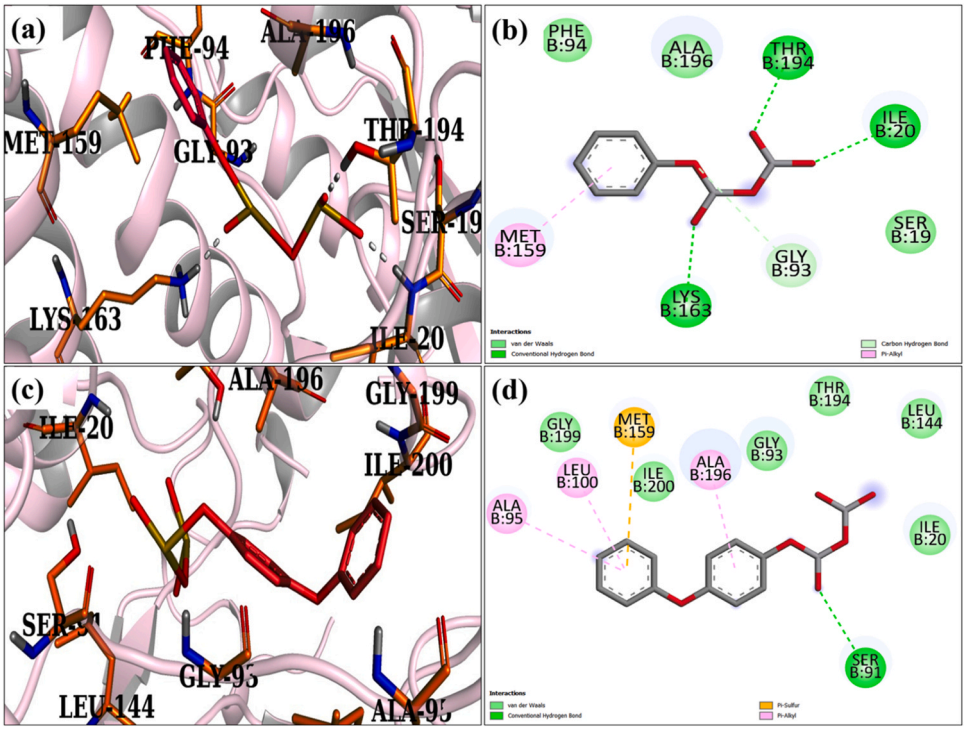


**Fig. 10.** (a) Binding interactions of CS-$V_2O_5$ (a (3D), b (2D)), and GO/CS-$V_2O_5$ NRs (c (3D), d (2D)) inside the active pocket of $FabI_{E.coli}$ complex.

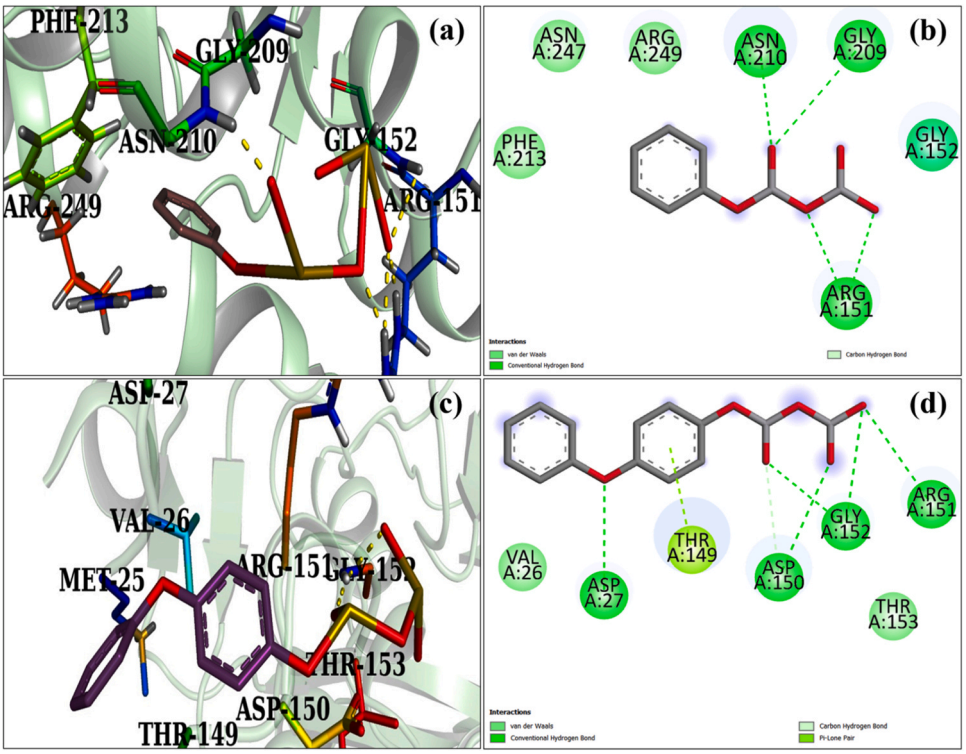


**Fig. 11.** (a) Binding interactions of CS-$V_2O_5$ (a (3D), b (2D)), and GO/CS-$V_2O_5$ NRs (c (3D), d (2D)) inside the active pocket of $FabI_{E.coli}$ complexFabH from *E.coli.*

The FabI and FabH enzymes in the fatty acid production pathway are major targets [78] and are investigated in this study. Docked complexes revealed their binding pattern in active region as well as proved their effectiveness against specific enzyme targets. In CS-$V_2O_5$, optimally docked area for $FabI_{E.coli}$ demonstrated H-bonding interactions with Thr194 and Ile20, Lys163, Gly 93, and Met159. A 4.19 binding score can be indicated in Fig. 10 (a,b). Similarly, GO/CS -$V_2O_5$ residues include pi-alkyl interactions with Ala95, Leu100, and Ala196; H-bond with Ser91 having a binding score of 5.37 (Fig. 10c-d).

The docking complex of CS-$V_2O_5$ exhibited H-bonding with Gly209, Asn210, and Arg 151, proclaimed in Fig. 11 (a,b). These CS-$V_2O_5$ NSs were considered as potent antagonists, inhibiting FabH enzyme's active region with a binding score of 2.74. The docking of GO/CS-$V_2O_5$ NRs revealed H-bonding interactions with Gly152, Arg151, and Asp150 along with 3.87 binding scores (Fig. 11c-d). Enzymatic activity terminates when ligand restricts substrate accessibility to the active site. GO/CS-$V_2O_5$ NSs had improved antibacterial action for *E. coli*, and in *silico* estimations for particular targets emphasized their possible binding patterns in active pocket, suggesting them as enzyme inhibitors.

## 4. Conclusion

The co-precipitation technique was utilized to prepare $V_2O_5$ and doped vanadium oxide nanorods with graphene oxide/carbon sphere doping concentrations of 3 and 6 wt%, respectively, to attain enhanced catalytic and bactericidal properties along with molecular docking analysis. SAED investigations supported formation of polycrystalline nature of synthesized nanorods. Furthermore, XRD analysis revealed the presence of orthorhombic and tetragonal structures with high phase purity, crystallinity, and crystallite size values measured at 55, 65, 78, and 83 nm, respectively. The TEM results showed that prepared nanorods possessed sheet-like morphology. Additionally, EDS and mapping analysis confirmed the elemental composition of the synthesized nanorods. FTIR spectra proclaimed the vibration bands V-O-V, which confirmed the production of $V_2O_5$. The optical absorption was noticed at 400 nm. With the incorporation of GO/CS, the redshift was observed, and a reduction in energy band gap of 3.1–2.8 eV was detected. The optical emission spectra show the least amount of electron-hole recombination as the intensity decreases with the addition of GO/CS. The dye was destroyed in a Fenton-like process in which RhB dye decomposed into byproducts such as $H_2O$ and $CO_2$. Compared to GO/CS, the pristine sample displayed promising degradation for RhB dye in different environments (neutral, acidic, and basic) at 88.89%, 89.85%, and 81.0%, respectively. In neutral medium, CS-doped (93.71%) sample degraded the dye most effectively. Furthermore, the bactericidal capability of the synthesized NRs was tested against *E. coli*, and the inhibition zones measured at high concentrations for high dosages were 3.75 mm. Molecular docking proposed potential mechanism for microbicidal effect of CS-$V_2O_5$ and GO/CS-$V_2O_5$ NRs towards FabI and FabH enzymes of *E. coli.*

## CRediT authorship contribution statement

**Muhammad Ikram**: Conceptualization, Investigation, Writing – original draft preparation, Supervision, Funding acquisition, Visualization. **Muhammad Shahid Ali**: Methodology, Formal analysis, Writing – review & editing. **Ali Haider**: Conceptualization, Resources. **Iram Shahzadi**: Conceptualization, Writing – review & editing, Investigation. **Muhammad Mustajab**: Data curation, Resources. **Anwar Ul-Hamid**: Methodology, Formal analysis. **Anum Shahzadi**: Investigation, Data curation. **Walid Nabgan**: Formal analysis, Conceptualization, Funding acquisition. **Mohammed M. Algaradah, Ahmed M. Fouda, Salamat Ali**: Conceptualization, Formal analysis, Writing – review & editing.

## Data availability

Data will be made available on request.

## Declaration of Competing Interest

The authors declare that they have no known competing financial interests or personal relationships that could have appeared to influence the work reported in this paper.

## Acknowledgment

Authors are thankful to higher education commission (HEC), Pakistan through NRPU 20–17615 and authors also extend their appreciation to the Deanship of Scientific Research at King Khalid University, Saudi Arabia for funding this work through Small Groups Project under Grant Number (RGP.1/248/44).

## References

[1] A.U. Khan, A.U. Khan, B. Li, M.H. Mahnashi, B.A. Alyami, Y.S. Alqahtani, A.O. Alqarni, Z.U.H. Khan, S. Ullah, M. Wasim, Q.U. Khan, W. Ahmad, Biosynthesis of silver capped magnesium oxide nanocomposite using Olea cuspidata leaf extract and their photocatalytic, antioxidant and antibacterial activity, Photo Photodyn. Ther. 33 (2021) 102153, https://doi.org/10.1016/j.pdpdt.2020.102153

[2] M. Jayapriya, K. Premkumar, M. Arulmozhi, K. Karthikeyan, One-step biological synthesis of cauliflower-like Ag/MgO nanocomposite with antibacterial, anticancer, and catalytic activity towards anthropogenic pollutants, Res. Chem. Intermed. 46 (2020) 1771–1788, https://doi.org/10.1007/s11164-019-04062-1

[3] A. Tkaczyk, K. Mitrowska, A. Posyniak, Synthetic organic dyes as contaminants of the aquatic environment and their implications for ecosystems: A review, Sci. Total Environ. 717 (2020) 137222, https://doi.org/10.1016/j.scitotenv.2020.137222

[4] B.S. Rathi, P.S. Kumar, D.V.N. Vo, Critical review on hazardous pollutants in water environment: Occurrence, monitoring, fate, removal technologies and risk assessment, Sci. Total Environ. 797 (2021) 149134, https://doi.org/10.1016/j.scitotenv.2021.149134

[5] W.B. Ayinde, M.W. Gitari, M. Muchindu, A. Samie, Biosynthesis of ultrasonically modified Ag-MgO nanocomposite and its potential for antimicrobial activity, J. Nanotechnol. 2018 (2018) 9537454, https://doi.org/10.1155/2018/9537454

[6] A. Chauhan, R. Verma, S. Kumari, A. Sharma, P. Shandilya, X. Li, K.M. Batoo, A. Imran, S. Kulshrestha, R. Kumar, Photocatalytic dye degradation and antimicrobial activities of Pure and Ag-doped ZnO using Cannabis sativa leaf extract, Sci. Rep. 10 (2020) 7881, https://doi.org/10.1038/s41598-020-64419-0

[7] S. Sreehari, N.S. George, L.M. Jose, S. Nandakumar, R.T. Subramaniam, A. Aravind, A review on 2D transition metal nitrides: Structural and morphological impacts on energy storage and photocatalytic applications, J. Alloy. Compd. 950 (2023) 169888, https://doi.org/10.1016/j.jallcom.2023.169888

[8] S. Sharma, S. Singh, U. Manhas, I. Qadir, A.K. Atri, D. Singh, Dramatic change in the photocatalytic activity of nanocrystalline La1-xNaxFeO3 (x = 0.0, 0.1, 0.2 and 0.3) perovskite oxides by the incorporation of Cu for effective removal of dyes, J. Alloy. Compd. 955 (2023) 170150, https://doi.org/10.1016/j.jallcom.2023.170150

[9] A. Bari, M. Ikram, A. Haider, A. Ul-Hamid, J. Haider, I. Shahzadi, G. Nazir, A. Shahzadi, M. Imran, A. Ghaffar, Evaluation of bactericidal potential and catalytic dye degradation of multiple morphology based chitosan/polyvinylpyrrolidone-doped bismuth oxide nanostructures, Nanoscale Adv. 4 (2022) 2713–2728, https://doi.org/10.1039/d2na00105e

[10] B.B. Garcia, G. Lourinho, P. Romano, P.S.D. Brito, Photocatalytic degradation of swine wastewater on aqueous TiO2 suspensions: optimization and modeling via Box-Behnken design, Heliyon 6 (2020) e03293, https://doi.org/10.1016/j.heliyon.2020.e03293

[11] A. Fouda, S.S. Salem, A.R. Wassel, M.F. Hamza, T.I. Shaheen, Optimization of green biosynthesized visible light active CuO/ZnO nano-photocatalysts for the degradation of organic methylene blue dye, Heliyon 6 (2020) e04896, https://doi.org/10.1016/j.heliyon.2020.e04896

[12] Y. Subramanian, V. Ramasamy, R.J. Karthikeyan, G.R. Srinivasan, D. Arulmozhi, R.K. Gubendiran, M. Sriramalu, Investigations on the enhanced dye degradation activity of heterogeneous BiFeO3–GdFeO3 nanocomposite photocatalyst, Heliyon 5 (2019) e01831, https://doi.org/10.1016/j.heliyon.2019.e01831

[13] S.A. Mohammed, L. Al Amouri, E. Yousif, A.A. Ali, F. Mabood, H.F. Abbas, S. Alyaqoobi, Synthesis of NiO:V2O5 nanocomposite and its photocatalytic efficiency for methyl orange degradation, Heliyon 4 (2018) e00581, https://doi.org/10.1016/j.heliyon.2018.e00581

[14] A. Mishra, A. Panigrahi, P. Mal, S. Penta, G. Padmaja, G. Bera, P. Das, P. Rambabu, G.R. Turpu, Rapid photodegradation of methylene blue dye by rGO- V2O5 nano composite, J. Alloy. Compd. 842 (2020) 155746, https://doi.org/10.1016/j.jallcom.2020.155746

[15] W. Xue, X. Hu, E. Liu, J. Fan, Novel reduced graphene oxide-supported Cd 0.5 Zn 0.5 S/g-C 3 N 4 Z-scheme heterojunction photocatalyst for enhanced hydrogen evolution, Appl. Surf. Sci. 447 (2018) 783–794, https://doi.org/10.1016/j.apsusc.2018.04.048

[16] K.C. Devarayapalli, K. Lee, H.B. Do, N.N. Dang, K. Yoo, J. Shim, S.V. Prabhakar Vattikuti, Mesostructured g-C3N4 nanosheets interconnected with V2O5 nanobelts as electrode for coin-cell-type-asymmetric supercapacitor device, Mater. Today Energy 21 (2021) 100699, https://doi.org/10.1016/j.mtener.2021.100699

[17] S. Vattikuti, A. Police, J. Shim, C. Byon, In situ fabrication of the Bi2O3–V2O5 hybrid embedded with graphitic carbon nitride nanosheets: oxygen vacancies mediated enhanced visible-light–driven, App, Surf. Sci. 447 (2018) 740–756, https://doi.org/10.1016/j.apsusc.2018.04.040

[18] Y. Xie, S.J. Li, J.P. Huang, R. Qiu, Z.Q. Liu, N. Li, Strengthening Co[sbnd]Co bond by copper doping in Co9S8 coupled with nitrogen-doped carbon sphere for enhancing the catalytic activity of oxygen reaction, J. Alloy. Compd. 921 (2022) 166076, https://doi.org/10.1016/j.jallcom.2022.166076

[19] M. Zhao, Y. Yang, Z. Zha, S. Cui, Y. Li, J. Yang, Enhanced photocatalytic performance of layered carbon microsphere/BiOCl composite with oxygen vacancies, J. Alloy. Compd. 928 (2022) 167068, https://doi.org/10.1016/j.jallcom.2022.167068

[20] A.A. Farghali, S.I. El-Dek, Physical and chemical aspects of metal oxide-carbon composites, Met. Oxide-Carbon Hybrid Mater. Synth. Prop. Appl. Elsevier, 2022, pp. 3–24, https://doi.org/10.1016/B978-0-12-822694-0.00008-9

[21] A.S.R.A. Subki, M.H. Mamat, M.Z. Musa, M.H. Abdullah, I.B. Shameem Banu, N. Vasimalai, M.K. Ahmad, N. Nafarizal, A.B. Suriani, A. Mohamad, M.D. Birowosuto, M. Rusop, Effects of varying the amount of reduced graphene oxide loading on the humidity sensing performance of zinc oxide/reduced graphene oxide nanocomposites on cellulose filter paper, J. Alloy. Compd. 926 (2022) 166728, https://doi.org/10.1016/j.jallcom.2022.166728

[22] N.C. Joshi, P. Gururani, Advances of graphene oxide based nanocomposite materials in the treatment of wastewater containing heavy metal ions and dyes, Curr. Res. Green. Sustain. Chem. 5 (2022), https://doi.org/10.1016/j.crgsc.2022.100306

[23] L. Ge, M. Zhang, R. Wang, N. Li, L. Zhang, S. Liu, T. Jiao, Fabrication of CS/GA/RGO/Pd composite hydrogels for highly efficient catalytic reduction of organic pollutants, RSC Adv. 10 (2020) 15091–15097, https://doi.org/10.1039/d0ra01884h

[24] Y. Guo, G. Xu, X. Yang, K. Ruan, T. Ma, Q. Zhang, J. Gu, Y. Wu, H. Liu, Z. Guo, Significantly enhanced and precisely modeled thermal conductivity in polyimide nanocomposites with chemically modified graphene: Via in situ polymerization and electrospinning-hot press technology, J. Mater. Chem. C. 6 (2018) 3004–3015, https://doi.org/10.1039/c8tc00452h

[25] P. Raizada, A. Sudhaik, P. Singh, Photocatalytic water decontamination using graphene and ZnO coupled photocatalysts: A review, Mater. Sci. Energy Technol. 2 (2019) 509–525, https://doi.org/10.1016/j.mset.2019.04.007

[26] R.K. Mandal, S. Kundu, S. Sain, S.K. Pradhan, Enhanced photocatalytic performance of V2O5-TiO2 nanocomposites synthesized by mechanical alloying with morphological hierarchy, N. J. Chem. 43 (2019) 2804–2816, https://doi.org/10.1039/c8nj05576a

[27] M. Ikram, A. Rafiq Butt, A. Fatima, I. Shahzadi, A. Haider, A. Ul-Hamid, T. Alshahrani, W. Nabgan, Graphitic-carbon nitride and poly acrylic acid doped vanadium oxide for efficient catalytic and antimicrobial activity: In silico molecular docking studies, J. Photochem. Photobiol. A Chem. 443 (2023) 114835, https://doi.org/10.1016/j.jphotochem.2023.114835

[28] A. Manohar, J. Park, D.D. Geleta, C. Krishnamoorthi, R. Thangam, H. Kang, J. Lee, Synthesis and characterization of ZnO nanoparticles for photocatalysis, antibacterial and cytotoxicity in kidney cancer (A498) cell lines, J. Alloy. Compd. 874 (2021) 159868, https://doi.org/10.1016/j.jallcom.2021.159868

[29] F. Adzitey, S. Yussif, R. Ayamga, S. Zuberu, F. Addy, G. Adu-Bonsu, N. Huda, R. Kobun, Antimicrobial Susceptibility and Molecular Characterization of Escherichia coli Recovered from Milk and Related Samples, Microorganisms 10 (2022) 1335, https://doi.org/10.3390/microorganisms10071335

[30] J.H. Jorgensen, J.D. Turnidge, Susceptibility test methods: dilution and disk diffusion methods, Man. Clin. Microbiol. ASM Press, 2015, pp. 1253–1273, https://doi.org/10.1128/9781555817381.ch71

[31] B.A. Iwalokun, A. Ogunledun, D.O. Ogbolu, S.B. Bamiro, J. Jimi-Omojola, In vitro antimicrobial properties of aqueous garlic extract against multidrug-resistant bacteria and Candida species from Nigeria, J. Med. Food 7 (2004) 327–333, https://doi.org/10.1089/jmf.2004.7.327

[32] A. Haider, M. Ijaz, M. Imran, M. Naz, H. Majeed, J.A. Khan, M.M. Ali, M. Ikram, Enhanced bactericidal action and dye degradation of spicy roots' extract-incorporated fine-tuned metal oxide nanoparticles, Appl. Nanosci. 10 (2020) 1095–1104, https://doi.org/10.1007/s13204-019-01188-x

[33] A. Haider, M. Ijaz, S. Ali, J. Haider, M. Imran, H. Majeed, I. Shahzadi, M.M. Ali, J.A. Khan, M. Ikram, Green Synthesized Phytochemically (Zingiber officinale and Allium sativum) Reduced Nickel Oxide Nanoparticles Confirmed Bactericidal and Catalytic Potential, Nanoscale Res. Lett. 15 (2020) 1–11, https://doi.org/10.1186/s11671-020-3283-5

[34] M. Ikram, A. Khalid, A. Shahzadi, A. Haider, S. Naz, M. Naz, I. Shahzadi, A. Ul-Hamid, J. Haider, W. Nabgan, A.R. Butt, Enhanced Photocatalytic Degradation with Sustainable CaO Nanorods Doped with Ce and Cellulose Nanocrystals: In Silico Molecular Docking Studies, ACS Omega 7 (2022) 27503–27515, https://doi.org/10.1021/acsomega.2c02732

[35] D.C. McKinney, C.J. Eyermann, R.F. Gu, J. Hu, S.L. Kazmirski, S.D. Lahiri, A.R. McKenzie, A.B. Shapiro, G. Breault, Antibacterial FabH Inhibitors with Mode of Action Validated in Haemophilus influenzae by in Vitro Resistance Mutation Mapping, ACS Infect. Dis. 2 (2016) 456–464, https://doi.org/10.1021/acsinfecdis.6b00053

[36] I. Shahzadi, M. Islam, H. Saeed, A. Haider, A. Shahzadi, J. Haider, N. Ahmed, A. Ul-Hamid, W. Nabgan, M. Ikram, H.A. Rathore, Formation of biocompatible MgO/cellulose grafted hydrogel for efficient bactericidal and controlled release of doxorubicin, Int. J. Biol. Macromol. 220 (2022) 1277–1286, https://doi.org/10.1016/j.ijbiomac.2022.08.142

[37] I. Shahzadi, M. Islam, H. Saeed, A. Shahzadi, J. Haider, A. Haider, M. Imran, H.A. Rathore, A. Ul-Hamid, W. Nabgan, M. Ikram, Facile synthesis of copolymerized cellulose grafted hydrogel doped calcium oxide nanocomposites with

improved antioxidant activity for anti-arthritic and controlled release of doxorubicin for anti-cancer evaluation. Int. J. Biol. Macromol. 235 (2023) 123874https://doi.org/10.1016/j.ijbiomac.2023.123874.
[38] M. Shanmugam, A. Alsalme, A. Alghamdi, R. Jayavel, Enhanced photocatalytic performance of the graphene-V2O5 nanocomposite in the degradation of methylene blue dye under direct sunlight, ACS Appl. Mater. Interfaces 7 (2015) 14905–14911, https://doi.org/10.1021/acsami.5b02715
[39] M. Ihsan, Q. Meng, L. Li, D. Li, H. Wang, K.H. Seng, Z. Chen, S.J. Kennedy, Z. Guo, H.K. Liu, V2O5/Mesoporous Carbon Composite as a cathode material for lithium-ion batteries, Electrochim. Acta 173 (2015) 172–177, https://doi.org/10.1016/j.electacta.2015.05.060
[40] N.D. Mohd Said, M.Z. Sahdan, N. Nayan, H. Saim, F. Adriyanto, A.S. Bakri, M. Morsin, Difference in structural and chemical properties of sol-gel spin coated Al doped TiO2, y doped TiO2 and Gd doped TiO2 based on trivalent dopants, RSC Adv. 8 (2018) 29686–29697, https://doi.org/10.1039/c8ra03950j
[41] A. Kumar, P.P. Sahay, Influence of Ti doping on the microstructural and electrochromic properties of dip-coated nanocrystalline V2O5 thin films, J. Sol. -Gel Sci. Technol. 95 (2020) 34–51, https://doi.org/10.1007/s10971-020-05298-9
[42] R.K. Sharma, P. Kumar, G.B. Reddy, Synthesis of vanadium pentoxide (V2O5) nanobelts with high coverage using plasma assisted PVD approach, J. Alloy. Compd. 638 (2015) 289–297, https://doi.org/10.1016/j.jallcom.2015.02.178
[43] C. O'Dwyer, V. Lavayen, S.B. Newcomb, M.A. Santa Ana, E. Benavente, G. González, C.M. Sotomayor Torres, Vanadate Conformation Variations in Vanadium Pentoxide Nanostructures, J. Electrochem. Soc. 154 (2007) K29, https://doi.org/10.1149/1.2746556
[44] A. Talledo, B. Stjerna, C.G. Granqvist, Optical properties of lithium-intercalated V2O5-based films treated in CF4 gas, Appl. Phys. Lett. 65 (1994) 2774–2776, https://doi.org/10.1063/1.112559
[45] B. Etemadi, J. Mazloom, F.E. Ghodsi, Phase transition and surface morphology effects on optical, electrical and lithiation/delithiation behavior of nanostructured Ce-doped V2O5 thin films, Mater. Sci. Semicond. Process. 61 (2017) 99–106, https://doi.org/10.1016/j.mssp.2016.12.035
[46] K.M. Parida, N. Sahu, Visible light induced photocatalytic activity of rare earth titania nanocomposites, J. Mol. Catal. A Chem. 287 (2008) 151–158, https://doi.org/10.1016/j.molcata.2008.02.028
[47] J. Tang, Z. Zou, J. Ye, Photophysical and photocatalytic properties of AgInW2O 8, J. Phys. Chem. B 107 (2003) 14265–14269, https://doi.org/10.1021/jp0359891
[48] C.C. Wang, K.C. Chen, F.S. Shieu, H.C. Shih, Characterization and photoluminescence of V2O5@Pt core-shell nanostructures as fabricated by atomic layer deposition, Chem. Phys. Lett. 729 (2019) 24–29, https://doi.org/10.1016/j.cplett.2019.05.018
[49] P.S. Chauhan, K. Kumar, K. Singh, S. Bhattacharya, Fast decolorization of rhodamine-B dye using novel V2O5-rGO photocatalyst under solar irradiation, Synth. Met. 283 (2022) 116981, https://doi.org/10.1016/j.synthmet.2021.116981
[50] Y. Shi, A. Babatunde, B. Bockelmann-Evans, G. Webster, Influence of hydraulic regimes and Cl2/NH3-N mass ratios on the bacterial structure and composition in an experimental flow cell chloraminated drinking water system, Environ. Sci. Water Res. Technol. 5 (2019) 977–992, https://doi.org/10.1039/c9ew00015a
[51] A. Jenifer, M.L.S. Sastri, S. Sriram, Photocatalytic dye degradation of V2O5 Nanoparticles—An experimental and DFT analysis, Opt. (Stuttg. ) 243 (2021) 167148, https://doi.org/10.1016/j.ijleo.2021.167148
[52] M.M. Sajid, N.A. Shad, Y. Javed, S.B. Khan, Z. Zhang, N. Amin, H. Zhai, Preparation and characterization of Vanadium pentoxide (V2O5) for photocatalytic degradation of monoazo and diazo dyes, Surf. Interfaces 19 (2020), https://doi.org/10.1016/j.surfin.2020.100502
[53] P.S. Chauhan, K. Kumar, K. Singh, S. Bhattacharya, Fast decolorization of rhodamine-B dye using novel V2O5-rGO photocatalyst under solar irradiation, Synth. Met. 283 (2022) 116981, https://doi.org/10.1016/j.synthmet.2021.116981
[54] M. Ikram, A. Rafiq Butt, A. Fatima, I. Shahzadi, A. Haider, A. Ul-Hamid, T. Alshahrani, W. Nabgan, Graphitic-carbon nitride and poly acrylic acid doped vanadium oxide for efficient catalytic and antimicrobial activity: In silico molecular docking studies, J. Photochem. Photobiol. A Chem. 443 (2023) 114835, https://doi.org/10.1016/j.jphotochem.2023.114835
[55] A. Krishnan, P.V. Vishwanathan, A.C. Mohan, R. Panchami, S. Viswanath, A.V. Krishnan, Tuning of Photocatalytic Performance of CeO2-Fe2O3 Composite by Sn-doping for the Effective Degradation of Methlene Blue (MB) and Methyl Orange (MO) dyes, Surf. Interfaces 22 (2021) 100808, https://doi.org/10.1016/j.surfin.2020.100808
[56] K. Yu, S. Yang, H. He, C. Sun, C. Gu, Y. Ju, Visible light-driven photocatalytic degradation of rhodamine B over NaBiO3: Pathways and mechanism, J. Phys. Chem. A 113 (2009) 10024–10032, https://doi.org/10.1021/jp905173e
[57] L. Hu, F. Yang, W. Lu, Y. Hao, H. Yuan, Heterogeneous activation of oxone with CoMg/SBA-15 for the degradation of dye Rhodamine B in aqueous solution, Appl. Catal. B Environ. 134–135 (2013) 7–18, https://doi.org/10.1016/j.apcatb.2012.12.028
[58] L. Hu, H. Yuan, L. Zou, F. Chen, X. Hu, Adsorption and visible light-driven photocatalytic degradation of Rhodamine B in aqueous solutions by Ag@AgBr/SBA-15, Appl. Surf. Sci. 355 (2015) 706–715, https://doi.org/10.1016/j.apsusc.2015.04.166
[59] X. Zhao, Y. Zhu, Synergetic degradation of rhodamine B at a porous ZnWO4 film electrode by combined electro-oxidation and photocatalysis, Environ. Sci. Technol. 40 (2006) 3367–3372, https://doi.org/10.1021/es052029e
[60] S. Singh, S.L. Lo, Single-phase cerium oxide nanospheres: An efficient photocatalyst for the abatement of rhodamine B dye, Environ. Sci. Pollut. Res. 25 (2018) 6532–6544, https://doi.org/10.1007/s11356-017-0902-5
[61] A.A. Isari, A. Payan, M. Fattahi, S. Jorfi, B. Kakavandi, Photocatalytic degradation of rhodamine B and real textile wastewater using Fe-doped TiO 2 anchored on reduced graphene oxide (Fe-TiO 2 /rGO): Characterization and feasibility, mechanism and pathway studies, Appl. Surf. Sci. 462 (2018) 549–564, https://doi.org/10.1016/j.apsusc.2018.08.133
[62] T.S. Natarajan, M. Thomas, K. Natarajan, H.C. Bajaj, R.J. Tayade, Study on UV-LED/TiO2 process for degradation of Rhodamine B dye, Chem. Eng. J. 169 (2011) 126–134, https://doi.org/10.1016/j.cej.2011.02.066
[63] L. Liu, W.K. Meng, Y.S. Zhou, X. Wang, G.J. Xu, M.L. Wang, J.M. Lin, R.S. Zhao, B-Ketoenamine-linked covalent organic framework coating for ultra-high-performance solid-phase microextraction of polybrominated diphenyl ethers from environmental samples, Chem. Eng. J. 356 (2019) 926–933, https://doi.org/10.1016/j.cej.2018.09.081
[64] D. Xu, X. Sun, X. Zhao, L. Huang, Y. Qian, X. Tao, Q. Guo, Heterogeneous Fenton Degradation of Rhodamine B in Aqueous Solution Using Fe-Loaded Mesoporous MCM-41 as Catalyst, Water Air. Soil Pollut. 229 (2018) 1–9, https://doi.org/10.1007/s11270-018-3932-9
[65] Y. Liu, H. Guo, Y. Zhang, X. Cheng, P. Zhou, G. Zhang, J. Wang, P. Tang, T. Ke, W. Li, Heterogeneous activation of persulfate for Rhodamine B degradation with 3D flower sphere-like BiOI/Fe3O4 microspheres under visible light irradiation, Sep. Purif. Technol. 192 (2018) 88–98, https://doi.org/10.1016/j.seppur.2017.09.045
[66] S.M. Saleh, A.E.A.E. Albadri, M.A. Ben Aissa, A. Modwi, Fabrication of Mesoporous V2O5@g-C3N4 Nanocomposite as Photocatalyst for Dye Degradation, Crystals 12 (2022) 1766, https://doi.org/10.3390/cryst12121766
[67] K.K. Laali, W.J. Greves, S.J. Correa-Smits, A.T. Zwarycz, S.D. Bunge, G.L. Borosky, A. Manna, A. Paulus, A. Chanan-Khan, Novel fluorinated curcuminoids and their pyrazole and isoxazole derivatives: Synthesis, structural studies, Computational/Docking and in-vitro bioassay, J. Fluor. Chem. 206 (2018) 82–98, https://doi.org/10.1016/j.jfluchem.2017.11.013
[68] S.K. Jayaraj, V. Sadishkumar, T. Arun, P. Thangadurai, Enhanced photocatalytic activity of V2O5 nanorods for the photodegradation of organic dyes: A detailed understanding of the mechanism and their antibacterial activity, Mater. Sci. Semicond. Process. 85 (2018) 122–133, https://doi.org/10.1016/j.mssp.2018.06.006
[69] S. Ashraf, M.A. El-Morsy, N.S. Awwad, H.A. Ibrahium, Physicochemical changes of hydroxyapatite, V2O5, and graphene oxide composites for medical usages, J. Aust. Ceram. Soc. 58 (2022) 1399–1413, https://doi.org/10.1007/s41779-022-00735-0
[70] H. Chaudhary, K. Chaudhary, S. Zulfiqar, M.S. Saif, I.A. Alsafari, I. Shakir, P.O. Agboola, M. Safdar, M.F. Warsi, Fabrication of reduced Graphene Oxide supported Gd3+ doped V2O5 nanorod arrays for superior photocatalytic and antibacterial activities, Ceram. Int. 47 (2021) 32521–32533, https://doi.org/10.1016/j.ceramint.2021.08.146
[71] A.M. Azzam, M.A. Shenashen, M.M. Selim, A.S. Alamoudi, S.A. El-Safty, Hexagonal Mg(OH)2 Nanosheets as Antibacterial Agent for Treating Contaminated Water Sources, ChemistrySelect 2 (2017) 11431–11437, https://doi.org/10.1002/slct.201701956
[72] M. Ikram, I. Shahzadi, A. Haider, S. Hayat, J. Haider, A. Ul-Hamid, A. Shahzadi, W. Nabgan, S. Dilpazir, S. Ali, Improved catalytic activity and bactericidal behavior of novel chitosan/V2O5 co-doped in tin-oxide quantum dots, RSC Adv. 12 (2022) 23129–23142, https://doi.org/10.1039/d2ra03975c
[73] M. Ikram, A. Haider, M. Imran, J. Haider, S. Naz, A. Ul-Hamid, W. Nabgan, M. Mustajab, A. Shahzadi, I. Shahzadi, M.A. Raza, G. Nazir, Facile synthesis of starch and tellurium doped SrO nanocomposite for catalytic and antibacterial potential: In silico molecular docking studies, Int. J. Biol. Macromol. 221 (2022) 496–507, https://doi.org/10.1016/j.ijbiomac.2022.09.034
[74] E. Ragab, M. Shaban, A.A. Khalek, F. Mohamed, Design and characterization of PANI/starch/Fe2O3 bio composite for wastewater remediation, Int. J. Biol. Macromol. 181 (2021) 301–312, https://doi.org/10.1016/j.ijbiomac.2021.03.043
[75] P. Dash, S. Raut, M. Jena, B. Nayak, Harnessing the biomedical properties of ferromagnetic α-Fe2O3 NPs with a plausible formation mechanism, Ceram. Int. 46 (2020) 26190–26204, https://doi.org/10.1016/j.ceramint.2020.07.117
[76] Z. Mehmood, M. Ikram, M. Imran, A. Shahzadi, A. Haider, A. Ul-Hamid, W. Nabgan, J. Haider, S. Hayat, Z. officinale-doped silver/calcium oxide nanocomposites: Catalytic activity and antimicrobial potential with molecular docking analysis, Process Biochem 121 (2022) 635–646, https://doi.org/10.1016/j.procbio.2022.07.035
[77] M. Mustajab, M. Ikram, A. Haider, A. Ul-Hamid, W. Nabgan, J. Haider, R. Ghaffar, A. Shahzadi, A. Ghaffar, A. Saeed, Promising performance of polyvinylpyrrolidone-doped bismuth oxyiodide quantum dots for antibacterial and catalytic applications, Appl. Nanosci. 12 (2022) 2621–2633, https://doi.org/10.1007/s13204-022-02547-x
[78] M. Ikram, S. Abbasi, A. Haider, S. Naz, A. Ul-Hamid, M. Imran, J. Haider, A. Ghaffar, Bimetallic Ag/Cu incorporated into chemically exfoliated MoS2 nanosheets to enhance its antibacterial potential: In silico molecular docking studies, Nanotechnology 31 (2020) 275704, https://doi.org/10.1088/1361-6528/ab8087